EurJIC
European Journal of Inorganic Chemistry

Chemistry Europe
European Chemical Societies Publishing

Accepted Article

Title: Bis(pyrazolato) Bridged Diiron Complexes: Ferromagnetic Coupling in a Mixed-Valent HS-FeII/LS-FeIII Dinuclear Complex

Authors: Joanne W. L. Wong, Shao-An Hua, Serhiy Demeshko, Sebastian Dechert, Shengfa Ye, and Franc Meyer

To be cited as: *Eur. J. Inorg. Chem.* 10.1002/ejic.202000697

Link to VoR: https://doi.org/10.1002/ejic.202000697

WILEY-VCH

10.1002/ejic.202000697

WILEY-VCH

FULL PAPER

Bis(pyrazolato) Bridged Diiron Complexes: Ferromagnetic Coupling in a Mixed-Valent HS-Fe^{II}/LS-Fe^{III} Dinuclear Complex

Joanne W. L. Wong,[a] Shao-An Hua,[a] Serhiy Demeshko,[a] Sebastian Dechert,[a] Shengfa Ye,[b],[c] and Franc Meyer*[a]

Abstract: Using a new bis(tridentate) compartmental pyrazolate-centered ligand HL, the bis(pyrazolato)-bridged diiron complex $[L_2Fe^{II}_2][OTf]_2$ (**1**) and its singly oxidized mixed-valent congener $[L_2Fe^{II}Fe^{III}][OTf]_3$ (**2**) have been synthesized and structurally characterized. While **1** features two HS-Fe^{II} ions coordinated to two *cis*-axial pyridine moieties in a highly distorted octahedral environment, the metal ions in **2** are coordinated by the ligand strand in a *trans*-axial configuration. Very different Fe-N bond lengths and distinctly different coordination polyhedral are associated with pronounced valence localization in the case of **2**. The electronic structures and magnetic properties of **1** and **2** have been further investigated by Mössbauer spectroscopy and variable temperature magnetic susceptibility measurements. In the case of **1**, weak antiferromagnetic coupling is observed between the two HS-Fe^{II} ions (J = –0.6 cm^{-1}), while the HS-Fe^{II} and LS-Fe^{III} ions in **2** are ferromagnetically coupled (J = +5.2 cm^{-1}) to give an S_T = 5/2 ground state with significant zero-field splitting ($D_{Fe(II)}$ = 2.3 cm^{-1}). The findings are rationalized with the help of DFT computations.

Introduction

Chelating ligands with a central pyrazole bridging moiety are versatile building blocks for numerous coordination compounds with varying architectures and nuclearity.[1,2] A family of rigid and planar bis(tridentate) ligands HL^R (Scheme 1) that provide two terpy-type binding pockets has been beneficially used for creating rugged diruthenium water-oxidation catalysts[3,4] as well as self-assembled homometallic and heterometallic [2×2] grids.[3],[5]–[9] Specifically, Fe_4 grid complexes based on ligand scaffolds $[L^R]^-$ have shown multistability with respect to spin and redox states.[5,6,10] Many of the all-ferrous complexes $[Fe_4(L^R)_4]^{4+}$ show thermal spin crossover (SCO), and correlations have been established between structural parameters and the pattern of high-spin (HS) and low-spin (LS) metal ions in the tetranuclear grid. A high degree of cooperativity was found for the sequential spin-crossover (SCO) processes, which was attributed to strong elastic coupling and strain effects imparted by the rigid ligand scaffolds.[6,11] As a consequence, pronounced stabilization of a dimixed-spin configuration [HS-LS-HS-LS] was observed in which the identical sites are located at opposite corners of the grid. Spin states are correlated with structural distortion of the individual $\{FeN_6\}$ polyhedra from octahedral symmetry, quantified by inspecting $S(O_h)$ values from continuous shape measures.[12] Using fs transient optical-infrared absorption and x-ray emission spectroscopies in combination with DFT calculations, the ultrafast dynamics after photoexcitation in the solvated $[Fe_4(L^H)_4]^{4+}$ metallogrid as well as in a defect grid $[Fe_3(L^H)_2(HL^H)_2]^{4+}$ have been studied, and photocycles that involve metastable high-spin states have been established.[13,14] It was found that the nuclearity indeed has a profound impact on the photoinduced dynamics and that the energy-rich (hot) high-spin states live for several hundreds of nanoseconds, much longer than in their mononuclear congener $[Fe(terpy)_2]^{2+}$, which is likely associated with the coupling of radial and angular motions in the rigid [2×2] metallogrid.

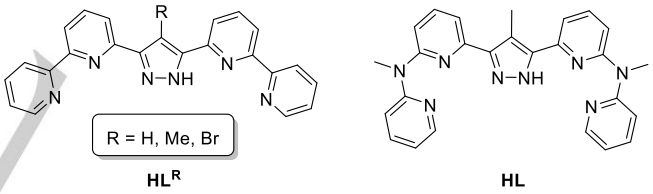

Scheme 1. Compartmental pyrazole-based ligands HL^R used in dinuclear Ru water oxidation catalysts and in [2 x 2] grid complexes; new ligand HL reported in this work, with additional NMe groups between the pyridine units.

Cooperativity effects in tetrairon [2×2] grid complexes of ligands $[L^R]^-$ also lead to pronounced stabilization of di-mixed-valence species with large comproportionation constants (>10^8).[5],[10] As in the mixed-spin systems, in these di-mixed-valence complexes metal ions of the same oxidation state are located at diagonally opposed vertices of the grid, resulting in a [Fe^{II}-Fe^{III}-Fe^{II}-Fe^{III}] configuration;[5] a similar situation has also been observed in di-mixed-valence tetrairon grids and squares with other types of ligand strands.[15–18] For complexes based on pyrazolate-bridging ligand scaffolds $[L^R]^-$, magnetic signatures evidenced ferromagnetic coupling between adjacent HS-Fe^{II} and LS-Fe^{III} ions.[5,10,18]

More generally, mixed-valent Fe^{II}/Fe^{III} iron complexes have been of interest in a variety of fields ranging from molecule-based magnetic materials to models of metalloprotein active sites.[19]–[21] The magnetic coupling as well as the extent of delocalization according to the Robin and Day classification[22] may vary widely and depend on, inter alia, the individual coordination

[a] Dr. J. W. L Wong, Dr. S.-A. Hua, Dr. S. Demeshko, Dr. S. Dechert, Prof. Dr. F. Meyer
Institut für Anorganische Chemie
Georg-August-Universität Göttingen
Tammannstrasse 4, D-37077 Göttingen (Germany)
E-mail: franc.meyer@chemie.uni-goettingen.de
Homepage: http://www.meyer.chemie.uni-goettingen.de

[b] Dr. S. Ye
Max-Planck Institut für Kohlenforschung
Stiftstraße 34-36, D-45470 Mülheim an der Ruhr (Germany)

[c] new address:
State Key Laboratory of Catalysis
Dalian Institute of Chemical Physics, Chinese Academy of Sciences
457 Zhongshan Road, Dalian 116023 (China)

Supporting information for this article is given via a link at the end of the document.

10.1002/ejic.202000697

environments and the nature of the bridging ligands.[23–26][27,28][29] Although the majority of metalloproteins and model complexes containing HS-Fe^{II} and HS-Fe^{III} ions display valence localized electronic structures and an S = ½ ground state,[30,31] some mixed valent systems show a propensity for ferromagnetic coupling through a double-exchange mechanism.[32] For example, ferromagnetic coupling was observed in $[Fe_2(OH)_3(tmtacn)_2]^{2+}$ (tmtacn = 1,4,7-trimethyltriazacyclononane) arising from significant overlap of the magnetic orbitals due to the small Fe···Fe distance of 2.51 Å, affording an overall S = 9/2 ground state.[33] In some cases, ferromagnetic coupling has also led to single molecule magnet (SMM) behaviour as observed in a self-assembled mixed-valent Fe^{II}/Fe^{III} tetranuclear star complex.[34]

In order to reduce the rigidity of the binucleating ligand scaffolds $[L^R]^-$ and to attenuate the elastic coupling between metal sites in their oligonuclear complexes, we prepared a new pyrazole-centered ligand with NMe groups between the pyridine subunits in the appended chelate arms (**HL**; see Scheme 1). This ligand modification was expected to enforce larger bite angles and to increase the ligand's flexibility for adapting to the stereoelectronic requirements of iron ions in different spin and redox states.[35,36] In contrast to ligands $[L^R]^-$, however, the new ligand $[L]^-$ was found to not form tetranuclear [2×2] grid complexes but dinuclear complexes $[L_2Fe_2]^{n+}$ instead. The synthesis, structure, redox and magnetic properties of the dinuclear Fe^{II} and the mixed-valent $Fe^{II}Fe^{III}$ complexes will be presented and discussed in this contribution.

Results and Discussion

The ligand HL and dinuclear $[L_2Fe^{II}_2]^{2+}$ complex 1. The new ligand **HL** was prepared following a multistep synthesis via key intermediates **I** and **II** (Scheme 2), adapting protocols previously developed for ligands HL^R.[6,10,37] Ester **I** and ketone **II** under basic conditions underwent a pseudo-Claison condensation to give a 1,3-diketone intermediate which was then methylated with excess CH_3I at the central pyrazolate C4 atom. The resulting bright yellow solid was subsequently treated with hydrazine monohydrate to give the desired ligand HL. Detailed procedures for the syntheses of **I**, **II** and **HL** as well as characterisation data are given in the Supporting Information (NMR spectra shown in Figures S1-S20).

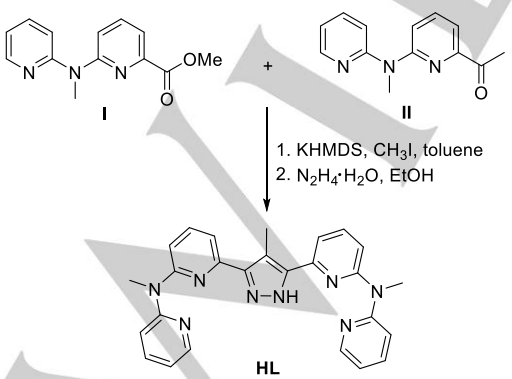

Scheme 2. Final steps of the synthesis of ligand **HL**.

The reaction of stoichiometric amounts of **HL** and $Fe^{II}(OTf)\cdot 2MeCN$ in the presence of Na^tOBu in dry MeCN, afforded the dinuclear complex $[L_2Fe^{II}_2](OTf)_2$ (**1**) as a yellow microcrystalline powder. This was further purified by slow diffusion of Et_2O into a solution of crude **1** in MeCN to give yellow-plate like crystals suitable for X-ray crystallography. The molecular structure of **1** (Figure 1) shows the presence of a diiron complex dication in which the metal ions are bridged by two pyrazolates and each Fe is found six-coordinate, hosted by two {N3} binding sites from the different ligand strands. **1** crystallizes in the orthorhombic space group *Pnnm* with high local symmetry (C_{2h}) of the dicationic $[L_2Fe^{II}_2]^{2+}$ complex. The average Fe-N bond lengths of 2.19 Å are consistent with HS-Fe^{II} ions. The overall distortion of the $\{FeN_6\}$ core from an ideal polyhedron can be described using Continuous Symmetry Measures (CSM).[12] The high value of $S(O_h)$ = 11.04 indicates strong deviation from octahedral symmetry while the small value of S(itp) = 2.94 indicates that the coordination sphere is in fact closer to trigonal prismatic (Table 1). The two Fe ions in **1** are separated by 4.35 Å, consistent with several reported dinuclear Fe^{II} complexes based on related ligands with a central triazole bridge, so-called PMRT-type ligands (PMRT is 4-substituted-3,5-bis{[(2-pyridylmethyl)-amino]methyl}-4H-1,2,4-triazole).[38]

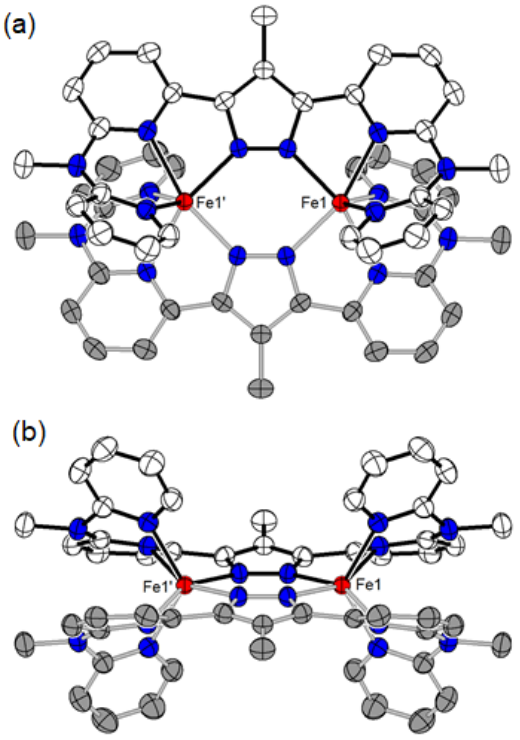

Figure 1. (a) Top and (b) side view of the dication of $[L_2Fe^{II}_2](OTf)_2$ (**1**) illustrating the *cis*-axial binding motif.

Table 1. Average Fe-N bond lengths and Continuous Symmetry Measures (CSM) for **1** and **2.**

		Fe-N [Å]	$S(O_h)$	S(itp)
1	Fe1	2.19	11.04	2.94
	Fe1'	2.19	11.04	2.94
2	Fe1	2.17	11.82	2.63
	Fe2	1.95	2.21	8.48

10.1002/ejic.202000697

Compound **1** was further characterized by electrospray ionization mass spectrometry (ESI-MS) and ^{1}H NMR spectroscopy. ESI-MS of **1** in MeCN afforded one dominant peak at *m/z* = 503 corresponding to the doubly charged cation $[L_2Fe^{II}_2]^{2+}$ confirming the stability of the dinuclear complex in MeCN solution (Figure 2, top). ^{1}H NMR spectroscopy of **1** in CD_3CN at rt indicated the presence of a highly symmetric species with nine resonances in the range from −3 ppm to +61 ppm, in accordance with the paramagnetic nature of the complex (Figure S21). Since through-space or dipolar nuclear relaxation is a dominating factor for the signal half width in case of small M···H distances in molecules with significant magnetic anisotropy, the broad signal at +61 ppm is tentatively assigned to the outermost H atom at the peripheral pyridines, which is in close proximity to the high-spin Fe^{II} ion. Due to the large linewidths, 2D NMR spectroscopy did not provide useful results for completing full spectral assignment. However, based on signal integrals the resonances at -2.79 ppm and +22.05 ppm can be assigned to the NMe groups and the CH_3 groups on the pyrazole backbone, respectively.

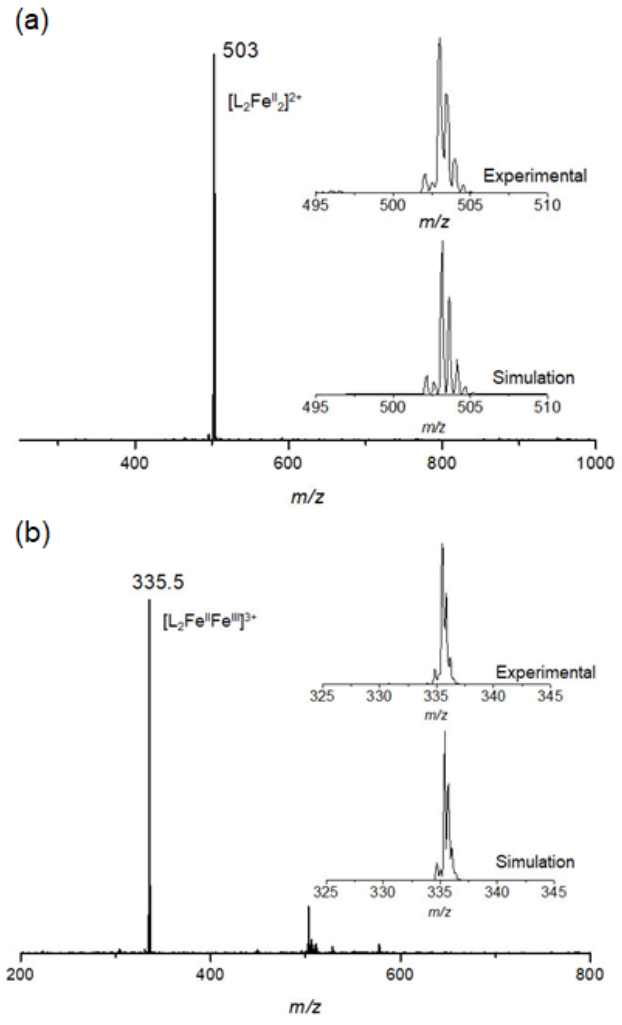

Figure 2. Positive ion ESI-MS of (a) $[L_2Fe^{II}_2][OTf]_2$ (**1**) in MeCN and (b) $[L_2Fe^{II}Fe^{III}](OTf)_3$ (**2**) in MeCN; the insets show the experimental and simulated isotopic distribution pattern for the doubly charged cation $[L_2Fe^{II}_2]^{2+}$ at *m/z* = 503 (a) and for the trication $[L_2Fe^{II}Fe^{III}]^{3+}$ at *m/z* = 335 (b).

The redox properties of $[L_2Fe^{II}_2](OTf)_2$ were investigated by cyclic voltammetry in MeCN (Figure 3). Two redox events at $E_{½}$ = 0.026 V and E_p^a = 0.590 V (all potentials vs. Fc/Fc^+; E_p^a is the anodic peak potential) are assigned to the $Fe^{II}_2/Fe^{II}Fe^{III}$ and $Fe^{II}Fe^{III}/Fe^{III}_2$ couples, respectively. Whereas the first process displays reversible behaviour based on $\Delta(E_p^a - E_p^c)$ = 88 mV and the linear dependence of i_{pf}/i_{pr} vs. the square root of scan rate ($v^{1/2}$; Figure 3), the second anodic process becomes more irreversible at slower scan rates most likely reflecting decomposition due to the highly charged nature of the twice oxidized $[L_2Fe^{III}_2]^{4+}$ complex (Figure S23). A large separation ΔE_p^a = 520 mV between the anodic peak potentials of the first and second oxidation indicate a pronounced thermodynamic stability of the mixed-valent $[L_2Fe^{II}Fe^{III}](OTf)_3$ complex ($K_c \approx 6.3 \times 10^8$) and suggest that it could be isolated after chemical oxidation.

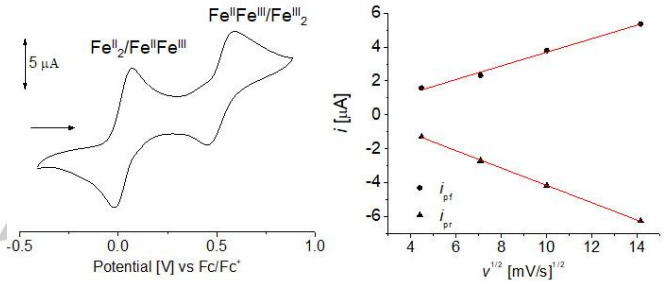

Figure 3. Cyclic voltammogram of **1** in MeCN at 100 mV/s with $[Bu_4N][PF_6]$ as the electrolyte (left) and and i_{pf}/i_{pr} vs $v^{1/2}$ for the oxidation of $[L_2Fe^{II}_2]]^{2+}$.

Mixed-valent complex 2. The formation of the mixed-valent and the doubly oxidized species was monitored using UV-Vis spectroelectrochemistry (UV-vis-SEC) by applying a potential of 0.12 V and 0.64 V for the first and second oxidative process, respectively (Figure 4). The initial spectrum of **1** shows an intense band at 332 nm (ε = 45.4 $mM^{-1}\cdot cm^{-1}$) originating from ligand-based $\pi \rightarrow \pi^*$ transitions along with a weaker broad band at 468 nm (ε = 1.1 $mM^{-1}\cdot cm^{-1}$), most likely corresponding to $Fe^{II} \rightarrow L^-$ metal-to-ligand charge transfer (MLCT) transitions. Applying a potential of 0.12 V caused the decrease in absorption of the band at 468 nm and concomitant rise of a new broad band at 634 nm, with isosbestic points at 413 nm and 542 nm. Further electrochemical oxidation to the doubly oxidized $[L_2Fe^{III}_2]^{4+}$ afforded a further increase in the band at 634 nm (Figure S25), suggesting that it might originate from a $L^- \rightarrow Fe^{III}$ ligand-to-metal charger transfer (LMCT) transition.

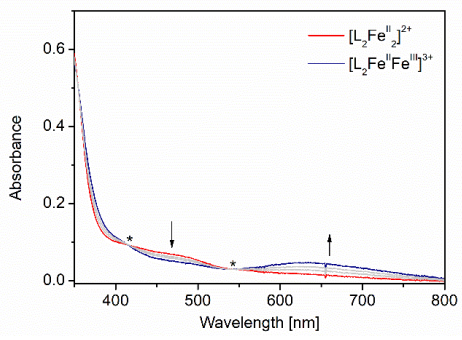

Figure 4. UV-Vis spectroelectrochemistry of **1** in MeCN with $[Bu_4N][PF_6]$ (0.1 M) as the electrolyte illustrating the electrochemical formation of the mixed valent $[L_2Fe^{II}Fe^{III}][OTf]_3$ (**2**); the asterisks indicate isosbestic points.

10.1002/ejic.202000697

Bulk synthesis of the singly oxidized complex $[L_2Fe^{II}Fe^{III}](OTf)_3$ (**2**) was performed by adding stoichiometric amounts of $Cu(OTf)_2$ to a solution of **1** in MeCN, affording a dark green solution. After 16 hours, the green solution was filtered and crystalline material of **2** was obtained by slow diffusion of Et_2O into the filtrate. Unfortunately, isolation of the twice oxidized complex $[L_2Fe^{III}{}_2](OTf)_4$ could not be achieved, likely because of its instability that is reflected in the CV data.

The molecular structure of the trication of **2**, determined by X-ray diffraction, is shown in Figure 5. The basic bis(pyrazolato)-bridged diiron core of **1** is retained in **2** with an essentially identical Fe···Fe distance of 4.35 Å, but the high symmetry observed in **1** is lost in mixed-valent **2**, due to the large structural changes that occur upon oxidation. Analysis of the Fe-N bond lengths reveal average bond lengths of 2.17 Å for Fe1 and 1.95 Å for Fe2, which are characteristic for HS-Fe^{II} and LS-Fe^{III} ions, respectively. $S(O_h)$ and S(itp) values are significantly different for the two metal ions: while the HS-Fe^{II} retains the coordination sphere that is strongly distorted from octahedral ($S(O_h)$ = 11.82) and better described as close to trigonal prismatic, the LS-Fe^{III} features a small $S(O_h)$ = 2.21 (Table 1) that reflects a close to octahedral coordination polyhedron.

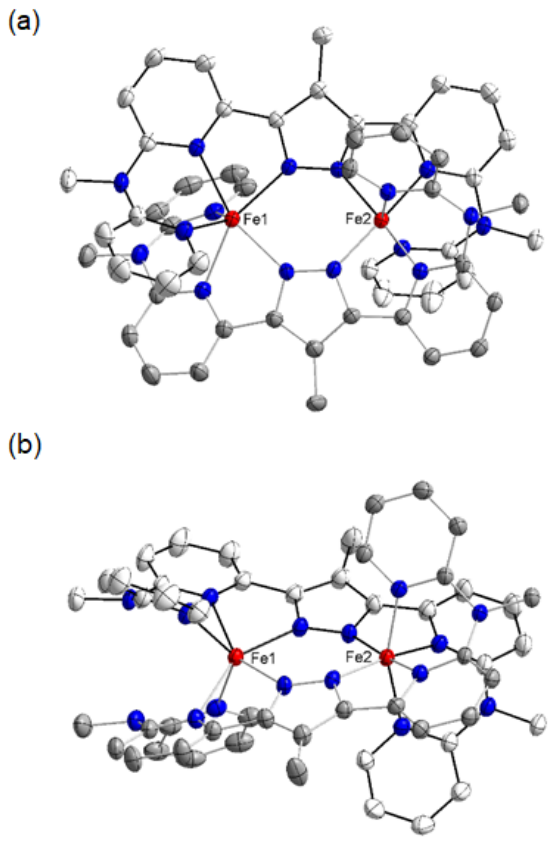

Figure 5. (a) Top and (b) side view of the trication of mixed valent $[L_2Fe^{II}Fe^{III}][OTf]_3$ (**2**) illustrating the *trans*-axial binding motif.

Interestingly, while the two terminal pyridine unit of each ligand strand are located on the same side of the bis(pyrazolato)-bridged diiron core in case of **1** (denoted *cis* hereafter), they are found on opposite sides (*trans*) in **2**. The latter binding motif was also observed for dinuclear complexes with PMRT-type ligands in which the NH linkages were replaced with sulfur atoms (PSRT ligands) as well as in a thiadiazole analogue of PMRT.[39],[40] The increased flexibility of the new bis(tridentate) ligand L^- compared to the more rigid ligands $[L^R]^-$, which results from the insertion of NMe moieties (or NH or S linkers in case PMRT and PSRT) in the chelate arms, obviously enables the ligand to adopt either the *cis* or the *trans* coordination mode in dinuclear complexes. One should note that the large structural changes accompanying oxidation of **1** to **2**, viz., the switch from a *cis* to a *trans* conformation of the ligand strands, likely requires transient ligand dissociation of the peripheral pyridine donors.

The positive ion ESI mass spectrum of a solution of **2** in MeCN is clearly distinct from the spectrum of **1** (Figure 2, bottom) and shows one dominant peak at *m/z* = 335.5 corresponding to the triply charged cation $[L_2Fe^{II}Fe^{III}]^{3+}$, thus confirming the stability of the oxidized diiron core in solution. The lack of signals for ions $[L_2Fe_2(OTf)]^{2+}$ or $[L_2Fe_2(OTf)_2]^+$ may suggest that ion pairing is not relevant in the polar solvent MeCN. The ^{1}H NMR spectrum of **2** at 298 K shows 13 signals in the range +50 - –2 ppm. Though the number of signals is less than the 15 resonances expected for a valence-localized molecule with C_2 symmetry, some resonances may be broadened beyond detection. These findings suggest that intervalence charge transfer (IVCT) between the Fe ions, which would lead to apparent C_{2h} symmetry, is slow on the NMR timescale, and that distinct sets of signals are observed for the ligand compartments at the HS-Fe^{II} and LS-Fe^{III} ions. This is in line with the very different Fe-N bond lengths and distinct coordination polyhedra for the HS-Fe^{II} and LS-Fe^{III} ions (viz. $S(O_h)$ = 11.82 versus 2.21), requiring large structural reorganization associated with IVCT that leads to pronounced valence localization in **2**. An alternative interpretation of the NMR spectra might be the presence of two different valence-delocalized isomers in solution with *cis*-axial or *trans*-axial arrangement of the two ligand strands (C_{2h} or D_2 symmetry, respectively); their interconversion may be slow because such process likely requires partial ligand dissociation. Variable temperature ^{1}H NMR spectra in the range 238 – 348 K show Curie behaviour with a linear dependence of the chemical shift $\delta(^1H)$ on the inverse temperature (Figure S22 and S23), but also significant broadening of several peaks upon cooling; subsequent warming of the sample restores the original spectrum observed at 298 K prior to cooling. Unfortunately, the broadness of all NMR peaks prevents reliable peak integration and recording of useful 2D NMR spectra. While the situation in solution remains ambiguous on the NMR timescale, we favour the interpretation in terms of prevented IVCT and localized valencies because slowly interconverting geometric isomers are not observed for homovalent **1**.

Electronic structures and magnetic properties and of 1 and 2.

The electronic structure and magnetic properties of **1** and **2** have been investigated using SQUID magnetometry and ^{57}Fe Mössbauer (MB) spectroscopy (Figure 6). The MB spectrum of solid **1** at 80 K shows a single doublet with an isomer shift of δ = 1.10 mm·s^{-1} and a quadruple splitting of ΔE_Q = 4.22 mm·s^{-1}, consistent with high-spin Fe^{II} ions (Table 2). The large electric field gradient at the Fe nuclei originates from the HS-d^6 configuration and the coordination environment that is quite distorted from a regular polyhedron. The slight difference in intensity between the two peaks of the doublet is likely caused by the texture of the sample.[41] Magnetic susceptibility measurements of solid **1** in the temperature 210 – 2 K revealed

an almost constant $\chi_M T$ value of 6.44 $cm^3 \cdot mol^{-1} \cdot K$ from 210 – 50 K consistent with two uncoupled HS-Fe^{II} ions (spin-only value of 6.00 $cm^3 \cdot mol^{-1} \cdot K$ for two S = 2 spin centers). Below 50 K, $\chi_M T$ decreases to reach 0.97 $cm^3 \cdot mol^{-1} \cdot K$ at 2 K, which is attributed to weak antiferromagnetic coupling between the two Fe^{II} ions. The experimental data was modelled according to the Heisenberg-Dirac-van-Vleck Hamiltonian (HDvV) shown in eq. 1 to give g_1 = g_2 = 2.11 and a coupling constant of J = –0.6 cm^{-1}.

$$\hat{H} = -2J\hat{S}_1\hat{S}_2 + g\mu_B \sum \vec{B}\,\vec{S}_i \qquad \text{(eq. 1)}$$

Although several related bis(triazole) bridged dinuclear Fe^{II} complexes with PMRT ligands were shown to exhibit spin crossover (SCO), the pronounced deviation from an octahedral coordination sphere in **1** prevents any thermal SCO and locks the Fe^{II} ions in their HS states.

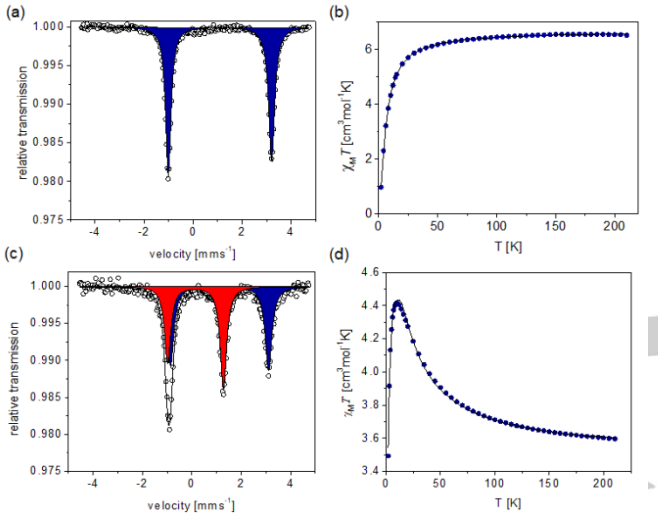

Figure 6. (a) ^{57}Fe MB spectrum (80 K) and (b) variable temperature magnetic susceptibility data of **1**; (c) ^{57}Fe MB spectrum (80 K) and (d) variable temperature magnetic susceptibility data of **2**.

Table 2. MB parameters for **1** and **2.**

	δ [mms^{-1}]	ΔE_Q [mms^{-1}]	relative intensity	spin state
1	1.10	4.22	100	HS-Fe^{II}
2	1.12	3.98	49	HS-Fe^{II}
	0.15	2.26	51	LS-Fe^{III}

DFT calculations show that an open-shell singlet state of **1** featuring two antiferromagnetically coupled Fe^{II} ions has the same energy as the corresponding S = 4 state. As depicted in Figure 7, the magnetic orbitals of the singlet state obtained by the corresponding orbital transformation[42] forms four spin-coupled pairs that represents the viable antiferromagnetic coupling pathways between the two Fe centers, yet all have nearly vanishing overlaps. On one hand, this can be readily traced back to the long Fe···Fe separation that essentially prevents their direct interactions. On the other hand, the metal-ligand interaction in **1** is rather ionic, as evidenced by all magnetic orbitals having predominant Fe 3d parentage (>90%) with negligible contributions from the ligands. Thus, the limited delocalization of the magnetic orbitals onto the bridging ligands largely suppresses any super-exchange interactions. As a consequence, although the magnetic orbitals are not orthogonal to each other, the exchange coupling in **1** is very weak, consistent with the experimental findings.

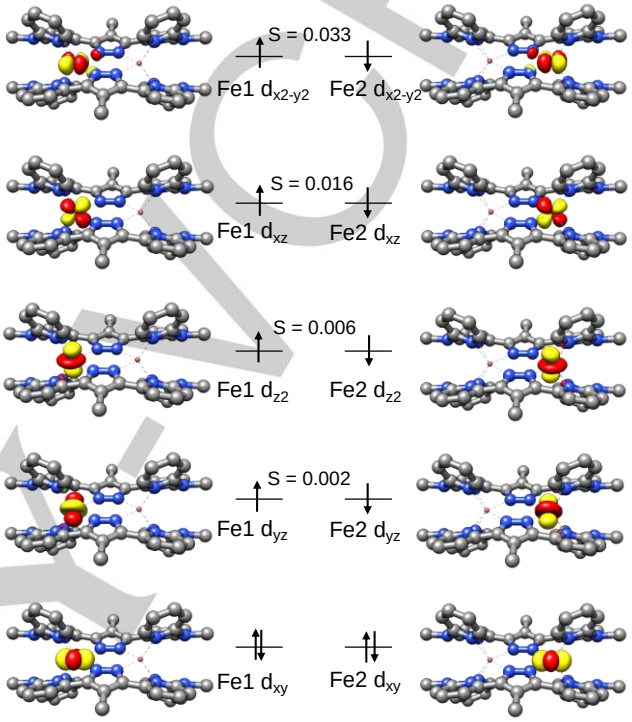

Figure 7. Molecular orbital diagram of the open-shell singlet state of complex **1**.

The ^{57}Fe MB spectrum of the mixed valent complex $[L_2Fe^{II}Fe^{III}](OTf)_3$ (**2**) shows two quadrupole doublets with an approximate 1:1 intensity ratio, in accordance with the presence of two different Fe ions and valence localization (Table 2). One doublet has parameters very similar to those of **1** (isomer shift of δ = 1.12 $mm \cdot s^{-1}$ and ΔE_Q = 3.98 $mm \cdot s^{-1}$), and it can be assigned to the HS-Fe^{II} ion. The second doublet has a much lower isomer shift of δ = 0.15 $mm \cdot s^{-1}$ and a smaller quadrupole splitting of ΔE_Q = 2.26 $mm \cdot s^{-1}$, which is characteristic for LS-Fe^{III}. These findings are fully consistent with the structural data obtained from X-ray diffraction which, based on the Fe-N bond lengths, suggested a HS-Fe^{II}/LS-Fe^{III} situation for **2**.

Accordingly the magnetic properties of mixed-valent **2** differ significantly from those of the parent dinuclear Fe^{II} compound **1**. At 210 K, a much lower $\chi_M T$ value of 3.60 $cm^3 \cdot mol^{-1}$ K is observed, close to the expected spin-only value of 3.375 $cm^3 \cdot mol^{-1} \cdot K$ for uncoupled S = ½ and S = 2 centers. As the temperature decreases, $\chi_M T$ gradually increases reaching a maximum value of 4.42 $cm^3 \cdot mol^{-1} \cdot K$ around 10 K. This magnetic signature reflects ferromagnetic coupling in **2**. Below 10 K, a steep decrease of $\chi_M T$ is observed, most likely due to zero-field splitting (ZFS). The experimental data was well modelled using the Heisenberg-Dirac-van-Vleck Hamiltonian that includes Zeeman splitting and an axial

10.1002/ejic.202000697

ZFS term (eq. 2), and best fit parameters are J = +5.2 cm^{-1}, $D_{Fe(II)}$ = 2.3 cm^{-1}, $g_{Fe(II)}$ = 2.02 and $g_{Fe(III)}$ = 2.10.

$$\hat{H} = -2J\hat{S}_1\hat{S}_2 + g\mu_B \sum \vec{B}\,\vec{S}_i + D_{Fe(II)}[\hat{S}_z^2 - \tfrac{1}{3}S(S+1)] \quad \text{(eq. 2)}$$

The Fe···Fe distance in **2** (4.35 Å) is much larger than in mixed-valent $[Fe_2(OH)_3(tmtacn)_2]^{2+}$ (2.51 Å), so that any direct interaction can be safely excluded, as in the case of **1**. Ferromagnetic coupling has previously been observed in mixed-valent [2 x 2] grids of ligands $[L^R]^-$ with similar Fe···Fe separations in which adjacent metal ions are bridged by a single pyrazolate:[5],[18] X-ray crystallography and Mössbauer spectroscopy of the mixed-valent grid $[L^H{}_4Fe^{II}{}_2Fe^{III}{}_2]^{6+}$ showed the presence of HS-Fe^{II} and LS-Fe^{III} ions situated at opposite corners, and magnetic measurements revealed ferromagnetic coupling between the HS-Fe^{II} and LS-Fe^{III} ions (J = +7.9 cm^{-1}).[5] Similarly, a related tetranuclear mixed valent grid $[L^{im}{}_4Fe^{II}{}_2Fe^{III}{}_2]^{6+}$ with peripheral imidazole units instead of pyridine moieties in the ligand strand also displayed ferromagnetic coupling via two intramolecular pathways with J_1 = +5.0 cm^{-1} and J_2 = +3.0 cm^{-1}; these values are comparable to the coupling observed in the mixed valent dinuclear complex **2**.[18] Partial orthogonality of the magnetic orbitals at the neighbouring HS-Fe^{II} and LS-Fe^{III} sites was proposed to give rise to these magnetic signatures of the mixed-valent $Fe^{II}{}_2Fe^{III}{}_2$ grid complexes. Substantial ferromagnetic coupling due to orthogonality of magnetic orbitals has further been observed in bis(pyrazolato) or pyrazolato/peroxido bridged dicopper(II) complexes with Cu-N-N-Cu or Cu-O-O-Cu torsion angles close to 90°, respectively.[43],[44]
To probe the origin of the magnetic signature of **2**, its S = 5/2 state attained by ferromagnetic coupling of a HS-Fe^{II} and a LS-Fe^{III} was analysed computationally by DFT. The S = 5/2 state was found nearly isoenergetic to the broken symmetry state in which the two fragments are antiferromagnetically coupled, with the former lying above by 0.1 kcal/mol; this energy gap is definitely far below the uncertainty range of DFT computations particularly in predicting reliable spin-state energetics of transition metal complexes.[45] Again, there is no symmetry restriction on the overlap of the magnetic orbital of the Fe2 center (Fe2 d_{xz}) with those of Fe1 (Figure 8). But the broken symmetry calculation at the sextet geometry estimated the overlap between Fe1 d_{xz} and Fe2 d_{xz} to be as low as 0.019 apparently due to the same reason elaborated for **1** (Figure S30), and this value was unaltered even when computed at the optimized geometry of the broken symmetry state. Despite this, upon oxidation the number of the antiferromagnetic coupling pathways is substantially reduced from four in **1** to one in **2**, because of the change of the Fe2 local spin state. At the same time, the ferromagnetic interactions between Fe2 d_{xz} with other magnetic orbitals of the Fe1 center, all of which are approximately orthogonal to each other, get enhanced. Both factors likely accounts for the preference of the ferromagnetic coupling in **2**.

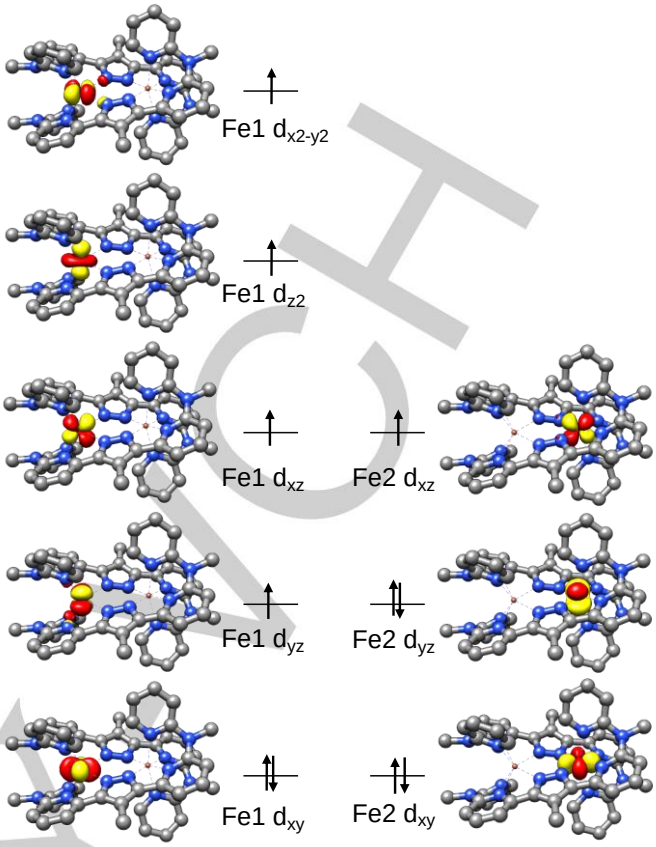

Figure 8. Molecular orbital diagram of the sextet state of complex **2**.

Conclusions

In conclusion, we have introduced a new pyrazolate-based bis(tridentate) compartmental ligand L^- that features elongated side arms with increased flexibility compared to the previously reported more rigid ligands $[L^R]^-$. Instead of tetrairon [2 x 2] grid complexes as observed for ligands $[L^R]^-$, the new ligand L^- forms a bis(pyrazolato)-bridged diiron complex $[L_2Fe^{II}{}_2](OTf)_2$ (**1**) with two HS-Fe^{II} (S = 2) ions that are weakly antiferromagnetically coupled (J = –0.6 cm^{-1}). Based on DFT calculations the lack of any significant exchange coupling in **1** is attributed to the negligible delocalization of the Fe(d) magnetic orbitals onto the bridging ligands. **1** can be oxidized twice, but only the singly oxidized mixed-valent complex $[L_2Fe^{II}Fe^{III}](OTf)_3$ (**2**) has been isolated and fully characterized whereas the twice oxidized species appears to be unstable on the CV timescale. Single crystal X-ray diffraction, ^{57}Fe Mößbauer spectroscopy and variable temperature magnetic susceptibility measurements reveal that the bis(pyrazolato) bridged diiron core is retained in **2** but shows major structural changes compared to **1**. Complex **2** contains a HS-Fe^{II} ion and a LS-Fe^{III} ion, and it is valence localized in the solid state and likely also in solution, based in ^{1}H NMR data. This is attributed to the very different Fe-N bond lengths and distinctly different coordination polyhedra for the HS-Fe^{II} ($S(O_h)$ = 11.82) and LS-Fe^{III} ($S(O_h)$ = 2.21) ions, which would require significant structural reorganization upon IVCT. Interestingly, the Fe ions in **1** are coordinated to the peripheral pyridine units in a *cis*-axial binding motif, while the Fe ions assume the *trans*-axial configuration in the mixed valent complex **2**, which suggests that transient ligand dissociation of the

peripheral pyridine donors must occur during transformation of **1** into **2**; however, the presence of two interconverting isomers in solution cannot be ruled out based on the available data. The HS-Fe^{II} and LS-Fe^{III} ions in **2** are ferromagnetically coupled (J = +5.2 cm^{-1}) to give an S_T = 5/2 ground state with significant zero-field splitting ($D_{Fe(II)}$ = 2.3 cm^{-1}). DFT computations indicate that the change in local spin state to LS-Fe^{III} at one of the metal ions significantly reduces the number of antiferromagnetic exchange pathway while ferromagnetic interactions get enhanced in **2** due to orthogonality of the magnetic orbitals.

Experimental Section

Materials and Methods.
All reactions were carried out under dry nitrogen using standard Schlenk techniques. Solvents were dried and degassed by standard procedures before use. Starting materials were purchased from commercial sources and used as received. The synthesis and characterization of the new ligand HL are described in the Supporting Information. UV–vis spectra of solutions were recorded with a Varian Cary 50 Bio Spectrophotometer at room temperature. NMR spectra were recorded on a Bruker Avance III 400. Chemical shifts (δ) are given in ppm relative to residual solvent signals of DMSO-d_6 and CD_3CN. Electron ionization (EI) mass spectra - were recorded with a Finnigan MAT 8200 and Electrospray ionization (ESI) mass spectra with a Finnigan MAT LCQ mass spectrometer. Cyclic voltammetry experiments were performed with the Gamry Interface 1010 E and analyzed using the Gamry Framework program. A three electrode setup was used: glassy carbon as the working electrode, Ag wire as the pseudo reference electrode and Pt wire as the counter electrode in CH_3CN/0.1 M Bu_4NPF_6. Ferrocene was used as the internal standard.

Mößbauer spectroscopy. Mößbauer spectra were recorded with a ^{57}Co source in a Rh matrix using an alternating constant acceleration *Wissel* Mössbauer spectrometer operated in the transmission mode and equipped with a *Janis* closed-cycle helium cryostat. Isomer shifts are given relative to iron metal at ambient temperature. Simulation of the experimental data was performed with the *Mfit* program using *Lorentzian* line doublets (E. Bill, Max-Planck Institute for Chemical Energy Conversion, Mülheim/Ruhr, Germany).

SQUID magnetometry. Temperature-dependent magnetic susceptibility measurements were carried out with a *Quantum-Design* MPMS-XL-5 SQUID magnetometer equipped with a 5 Tesla magnet in the range from 2 to 210 K in a magnetic field of 0.5 T. The polycrystalline samples were contained in a gel bucket, covered with a drop of low viscosity perfluoropolyether based inert oil Fomblin Y45 to fix the crystals, and fixed in a non-magnetic sample holder. The maximum measuring temperature of 210 K was chosen because of the pour point of the oil, in order to keep the oil in the frozen state and to avoid therefore the orientation of the crystals parallel to the magnetic field. Each raw data file for the measured magnetic moment was corrected for the diamagnetic contribution of the gel bucket and of the inert oil according to $M^{dia} = \chi_g \cdot m \cdot H$, with experimentally obtained gram susceptibility of the gel bucket ($\chi_g = -5.70 \cdot 10^{-7}$ emu/(g·Oe)) and of the oil ($\chi_g = -3.82 \cdot 10^{-7}$ emu/(g·Oe)). The molar susceptibility data were corrected for the diamagnetic contribution according to χ_M^{dia}(sample) = $-0.5 \cdot M \cdot 10^{-6}$ $cm^3 \cdot mol^{-1}$. Temperature-independent paramagnetism (*TIP*) was included according to $\chi_{calc} = \chi + TIP$. Before simulation, the experimental data were corrected for a *TIP* of $2200 \cdot 10^{-6}$ $cm^3 mol^{-1}$ or $1300 \cdot 10^{-6}$ $cm^3 mol^{-1}$ for **1** and **2**, respectively. Full-matrix diagonalization of the spin Hamiltonian for exchange coupling, zero-field splitting and Zeeman splitting was performed with the *julX* program.[37] Matrix diagonalization is done with the routine *ZHEEV* from the *LAPACK* numerical package. Parameter optimization is performed with the simplex routine *AMOEBA* from *NUMERICAL RECIPES*.

X-ray crystallography. Data were collected on a STOE IPDS II diffractometer (monochromated Mo-Kα radiation, λ = 0.71073 Å) by use of ω scans at –140 °C. The structures were solved with SHELXT and refined on F^2 using all reflections with SHELXL-18.[38] Crystal data and details of the data collections are provided in the Supporting Information (Tables S1 and S2). CCDC 2016435-2016436 contain the supplementary crystallographic data for this paper. These data can be obtained free of charge from The Cambridge Crystallographic Data Centre via http://www.ccdc.cam.ac.uk/data_request/cif.

DFT calculations. Geometry optimizations were performed with the B3LYP[46],[47] density functional. The def2-TZVP for the first coordination sphere and def2-SVP basis sets[48] for the remaining atoms were applied in combination with the auxiliary basis sets def2/J. [49] The RIJCOSX[50] approximations were used to accelerate the calculations. To account for non-covalent interactions, the atom-pairwise dispersion corrections with the Becke-Johnson damping scheme were employed.[51],[52] All calculations were performed by using the ORCA quantum chemical program package.[53]

Synthesis of $[L_2Fe^{II}_2](OTf)_2$ (1). HL (0.100 g, 0.223 mmol, 2 eq.) and NaO^{t}Bu (0.087 g, 0.905 mmol, 4 eq.) were dissolved in dry MeCN (10 mL) and the reaction mixture was stirred at room temperature for 45 minutes. Subsequently, $Fe^{II}(OTf)_2 \cdot 2MeCN$ (0.116 g, 0.266 mmol, 1.14 eq.) was added to give a deep red solution, which was stirred at room temperature. After 16 hours, bright yellow microcrystalline material of $[L_2Fe_2](OTf)_2$ precipitated out from solution (0.102 g, 0.085 mmol, 38% yield). Since ESI-MS, ^1H NMR spectroscopy and MB spectroscopy confirmed the purity of this crude product, most analytical measurements were conducted on the non-crystallized material. For X-ray diffraction analysis, single crystals were obtained by slow diffusion of Et_2O into a solution of $[L_2Fe_2](OTf)_2$ in MeCN. ^1H NMR (400 MHz, CD_3CN): δ(ppm) = 61.0 (s, 1 Ar-H), 49.4 (s, 1 Ar-H), 46.6 (s, 1 Ar-H), 37.8 (s, 1 Ar-H), 33.6 (s, 1 Ar-H), 22.1 (s, 2 NCH_3), 4.0 (s, 1 Ar-H), -2.0 (s, 1 Ar-H), -2.8 (s, 1 CH_3). ESI-MS (MeCN): *m/z* = 503 $[L^1{}_2Fe_2]^{2+}$. UV-vis (MeCN, 298 K): λ[nm] (ε[$M^{-1} \cdot cm^{-1}$]): 260 (72200), 302 (47500), 332 (45400), 468 (1080). ^{57}Fe MB: δ = 1.10 $mm \cdot s^{-1}$ (ΔE_Q = 4.22 $mm \cdot s^{-1}$).

Synthesis of $[L_2Fe^{II}Fe^{III}](OTf)_3$ (2). Complex **1** (0.050 g, 0.038 mmol, 1 eq.) was suspended in dry MeCN (6 mL) and a solution of $Cu(OTf)_2$ (0.014 g, 0.038 mmol, 1 eq.) in MeCN was added to give a green reaction mixture. This was stirred at room temperature for 16 hours under inert conditions and then filtered and evaporated to dryness. Slow diffusion of Et_2O into a solution of the crude product in MeCN yielded crystalline material of **2** (0.011 g, 0.008 mmol, 20% yield). ^1H NMR (400 MHz, CD_3CN): δ(ppm) = 48.46 (s, 1 Ar-H), 37.12 (s, 1 Ar-H), 25.27(s, 1 Ar-H), 24.70 (s, 1 Ar-H), 15.00 (s, 1 Ar-H), 14.70 (s, 1 Ar-H), 6.52 (s, 1 Ar-H), 4.44 (s, 1 CH_3), -1.18 (s, 2 CH_3). ESI-MS (MeCN): *m/z* = 335. UV-vis (MeCN, 298 K): λ[nm] (ε[$M^{-1} \cdot cm^{-1}$]): 256 (41450), 338 (20100), 620 (1510). ^{57}Fe MB: δ = 1.12 $mm \cdot s^{-1}$ (ΔE_Q = 3.98 $mm \cdot s^{-1}$), δ = 0.15 $mm \cdot s^{-1}$ (ΔE_Q = 2.26 $mm \cdot s^{-1}$).

Acknowledgements

Financial support by the Deutsche Forschungsgemeinschaft (DFG, German Research Foundation) 217133147/SFB 1073,

project B06 is gratefully acknowledged. S.Y. gratefully acknowledges the financial support from the Max-Planck Society, in particular, the joint work space of MPI-CEC and MPI-KOFO.

Keywords: dinuclear complexes • mixed-valent complexes • iron • magnetic properties • Mößbauer spectroscopy

[1] J. Klingele, S. Dechert, F. Meyer, *Coord. Chem. Rev.* **2009**, 2698–2741.

[2] K. E. Dalle, F. Meyer, *Eur. J. Inorg. Chem.* **2015**, 3391–3405.

[3] S. Neudeck, S. Maji, I. López, S. Dechert, J. Benet-Buchholz, A. Llobet, F. Meyer, *Inorg. Chem.* **2016**, 2508–2521.

[4] S. Neudeck, S. Maji, I. López, S. Meyer, F. Meyer, A. Llobet, *J. Am. Chem. Soc.* **2014**, 24–27.

[5] B. Schneider, S. Demeshko, S. Dechert, F. Meyer, *Angew. Chemie Int. Ed.* **2010**, 9274–9277.

[6] M. Steinert, B. Schneider, S. Dechert, S. Demeshko, F. Meyer, *Inorg. Chem.* **2016**, 2363–2373.

[7] M. Steinert, B. Schneider, S. Dechert, S. Demeshko, F. Meyer, *Angew. Chemie Int. Ed.* **2014**, 6135–6139.

[8] J. W. L. Wong, S. Demeshko, S. Dechert, F. Meyer, *Inorg. Chem.*, 2019, 13337–13345.

[9] J. Tong, S. Demeshko, M. John, S. Dechert, F. Meyer, *Inorg. Chem.* **2016**, 4362–4372.

[10] B. Schneider, S. Demeshko, S. Neudeck, S. Dechert, F. Meyer, *Inorg. Chem.* **2013**, 13230–13237.

[11] S. A. Borshch, E. M. Zueva, *Eur. J. Inorg. Chem.* **2013**, 1009–1014.

[12] S. Alvarez, D. Avnir, M. Llunell, M. Pinsky, *New J. Chem.* **2002**, 996–1009.

[13] M. A. Naumova, A. Kalinko, J. W. L. Wong, S. Alvarez Gutierrez, J. Meng, M. Liang, M. Abdellah, H. Geng, W. Lin, K. Kubicek, M. Biednov, F. Lima, A. Galler, P. Zalden, S. Checchia, P. A. Mante, J. Zimara, D. Schwarzer, S. Demeshko, V. Murzin, D. Gosztola, M. Jarenmark, J. Zhang, M. Bauer, M. L. Lawson Daku, D. Khakhulin, W. Gawelda, C. Bressler, F. Meyer, K. Zheng, S. E. Canton, *J. Chem. Phys.* **2020**, 214301.

[14] M. A. Naumova, A. Kalinko, J. W. L. Wong, M. Abdellah, H. Geng, E. Domenichini, J. Meng, S. A. Gutierrez, P. A. Mante, W. Lin, P. Zalden, A. Galler, F. Lima, K. Kubicek, M. Biednov, A. Britz, S. Checchia, V. Kabanova, M. Wulff, J. Zimara, D. Schwarzer, S. Demeshko, V. Murzin, D. Gosztola, M. Jarenmark, J. Zhang, M. Bauer, M. L. Lawson Daku, W. Gawelda, D. Khakhulin, C. Bressler, F. Meyer, K. Zheng, S. E. Canton, *J. Phys. Chem. Lett.* **2020**, 2133–2141.

[15] Y. Zhao, D. Guo, Y. Liu, C. He, C. Duan, *Chem. Commun.* **2008**, 5725–5727.

[16] K. V. Shuvaev, L. N. Dawe, L. K. Thompson, *Dalt. Trans.* **2010**, 4693–4707.

[17] T. Matsumoto, G. N. Newton, T. Shiga, S. Hayami, Y. Matsui, H. Okamoto, R. Kumai, Y. Murakami, H. Oshio, *Nat. Commun.* **2014**, 1–8.

[18] J. Tong, S. Demeshko, S. Dechert, F. Meyer, *Eur. J. Inorg. Chem.* **2017**, 4333–4343.

[19] A. Stubna, D. H. Jo, M. Costas, W. W. Brenessel, H. Andres, E. L. Bominaar, E. Münck, L. Que, *Inorg. Chem.* **2004**, 3067–3079.

[20] F. Li, M. Chakrabarti, Y. Dong, K. Kauffmann, E. L. Bominaar, E. Münck, L. Que, *Inorg. Chem.* **2012**, 2917–2929.

[21] C. J. White, A. L. Speelman, C. Kupper, S. Demeshko, F. Meyer, J. P. Shanahan, E. E. Alp, M. Hu, J. Zhao, N. Lehnert, *J. Am. Chem. Soc.* **2018**, 2562–2574.

[22] M. B. Robin, P. Day, *Adv. Inorg. Chem. Radiochem.* **1967**, 247–422.

[23] S. C. Payne, K. S. Hagen, *J. Am. Chem. Soc.* **2000**, 6399–6410.

[24] J. H. Satcher, M. W. Droege, M. M. Olmstead, A. L. Balch, *Inorg. Chem.* **2001**, 1454–1458.

[25] S. Chardon-Noblat, O. Horner, B. Chabut, F. Avenier, N. Debaecker, P. Jones, J. Pécaut, L. Dubois, C. Jeandey, J. L. Oddou, A. Deronzier, J. M. Latour, *Inorg. Chem.* **2004**, 1638–1648.

[26] A. Majumdar, U. P. Apfel, Y. Jiang, P. Moënne-Loccoz, S. J. Lippard, *Inorg. Chem.* **2014**, 167–181.

[27] E. Gouré, G. Thiabaud, M. Carboni, N. Gon, P. Dubourdeaux, R. Garcia-Serres, M. Clémancey, J. L. Oddou, A. Y. Robin, L. Jacquamet, L. Dubois, G. Blondin, J. M. Latour, *Inorg. Chem.* **2011**, 6408–6410.

[28] E. Gouré, M. Carboni, A. Troussier, P. Dubourdeaux, M. Clémancey, N. Gon, R. Balasubramanian, C. Lebrun, J. Pécaut, G. Blondin, J. M. Latour, *Inorg. Chem.* **2015**, 6257–6266.

[29] M. Van Der Meer, Y. Rechkemmer, F. D. Breitgoff, R. Marx, P. Neugebauer, U. Frank, J. Van Slageren, B. Sarkar, *Inorg. Chem.* **2016**, 11944–11953.

[30] G. Blondin, J. J. Girerd, *Chem. Rev.* **1990**, 1359–1376.

[31] E. I. Solomon, D. W. Randall, T. Glaser, *Coord. Chem. Rev.* **2000**, 595–632.

[32] S. Hazra, S. Sasmal, M. Fleck, F. Grandjean, M. T. Sougrati, M. Ghosh, T. D. Harris, P. Bonville, G. J. Long, S. Mohanta, *J. Chem. Phys.* **2011**, 174507.

[33] D. R. Gamelin, E. L. Bominaar, M. L. Kirk, K. Wieghardt, E. I. Solomon, *J. Am. Chem. Soc.* **1996**, 8085–8097.

[34] D. Sertphon, P. Harding, K. S. Murray, B. Moubaraki, N. F. Chilton, S. Hill, J. Marbey, H. Adams, C. G. Davies, G. N. L. Jameson, D. J. Harding, *Dalt. Trans.* **2018**, 7118–7122.

[35] K. MacK, A. Wünsche Von Leupoldt, C. Förster, M. Ezhevskaya, D. Hinderberger, K. W. Klinkhammer, K. Heinze, *Inorg. Chem.* **2012**, 7851–7858.

[36] A. K. C. Mengel, C. Bissinger, M. Dorn, O. Back, C. Förster, K. Heinze, *Chem. - A Eur. J.* **2017**, 7920–7931.

[37] J. I. Van Der Vlugt, S. Demeshko, S. Dechert, F. Meyer, *Inorg. Chem.* **2008**, 1576–1585.

[38] R. W. Hogue, S. Singh, S. Brooker, *Chem. Soc. Rev.* **2018**, 7303–7338.

[39] R. W. Hogue, H. L. C. Feltham, R. G. Miller, S. Brooker, *Inorg. Chem.* **2016**, 4152–4165.

[40] C. F. Herold, S. I. Shylin, E. Rentschler, *Inorg. Chem.* **2016**, 6414–6419.

[41] P. Gütlich, B. Bill, A. X. Trautwein, *Mössbauer Spectroscopy and Transition Metal Chemistry: Fundamentals and Applications*, Springer-Verlag: Berlin, **2011**.

[42] S. Ye, C. Y. Geng, S. Shaik, F. Neese, *Phys. Chem. Chem. Phys.* **2013**, 8017–8030.

[43] L. K. Frensch, K. Pröpper, M. John, S. Demeshko, C. Brückner, F. Meyer, *Angew. Chemie - Int. Ed.* **2011**, 1420–1424.

[44] N. Kindermann, E. Bill, S. Dechert, S. Demeshko, E. J. Reijerse, F. Meyer, *Angew. Chemie - Int. Ed.* **2015**, 1738–1743.

[45] S. Ye, F. Neese, *Inorg. Chem.* **2010**, 772–774.

[46] A. D. Becke, *J. Chem. Phys.* **1993**, 5648–5652.

[47] C. T. Lee, W. T. Yang, R. G. Parr, *Phys. Rev. B.* **1988**, 785–789.

[48] F. Weigend, R. Ahlrichs, *Phys. Chem. Chem. Phys.* **2005**, 3297.

[49] F. Weigend, *Phys. Chem. Chem. Phys*. **2006**, 1057.

[50] F. Neese, F. Wennmohs, H. A., U. Becker, *Chem. Phys.* **2009**, 98–109.

[51] S. Grimme, S. Ehrlich, L. Goerigk, *J. Comput. Chem.* **2011**, 1456–1465.

[52] S. Grimme, J. Antony, S. Ehrlich, H. Kreig, *J. Chem. Phys*. **2010**, 154104.

[53] F. Neese, *WIREs Comput. Mol. Sci.* **2018**, e1327.

10.1002/ejic.202000697

Entry for the Table of Contents

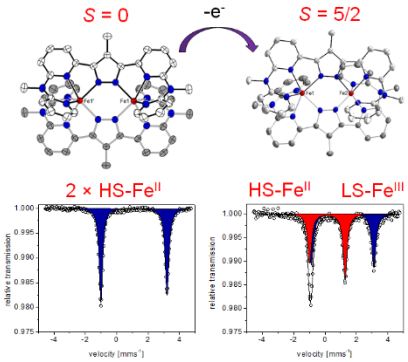

Trapped mixed-valence: Dinuclear iron complexes of a new pyrazolate-based ligand with flexible side arms were synthesized in both the Fe^{II}_2 and mixed-valent $Fe^{II}Fe^{III}$ forms. Upon oxidation, large structural changes were observed, associated with a high-spin to low-spin transition and charge localization. The different magnetic signatures of the two compounds were evidenced by a suite of experimental methods and investigated by DFT calculations.